MDPI

Article

Impact of Temperature on the Tensile Properties of Hypereutectic High-Entropy Alloys

Wei Jiang [1,2], Shuaishuai Wu [1,2], Xuehui Yan [1,2], Haochen Qiu [1,2,3], Shengli Guo [1,2,3], Baohong Zhu [1,2,3,*] and Hanjun Zhang [1,2,3]

1   GRIMAT Engineering Institute Co., Ltd., Beijing 101407, China; wjiang111@126.com (W.J.);
    wushuaishuai@grinm.com (S.W.); yanxuehui@grinm.com (X.Y.); qiuhaochen@grinm.com (H.Q.);
    guoshengli@grinm.com (S.G.); zhanghanjun7549@163.com (H.Z.)
2   China GRINM Group Corporation Limited, Beijing 100088, China
3   General Research Institute for Nonferrous Metals, Beijing 100088, China
*   Correspondence: zhubh@grinm.com

Abstract: Eutectic high-entropy alloys (EHEAs) can achieve a balance of high strength and ductility. It has been found that the mechanical properties of hypoeutectic high-entropy alloys are superior to those of EHEAs. In this work, hypereutectic $Al_{1.1}CoCrFeNi_{2.1}$ alloy was prepared, and the mechanical properties in a wide temperature range were studied. The presence of both soft ordered $L1_2$ and hard BCC (B_2) phases results in a combination of ductile and brittle fracture modes. The $Al_{1.1}CoCrFeNi_{2.1}$ hypereutectic high-entropy alloy contains more primary soft $L1_2$ phases, which ensure excellent ductility. Moreover, the Orowan by-passing mechanism caused by the B_2 precipitates increases in the strength of the alloy for low-temperature tensile tests ($-100\,°C$ and $23 \pm 2\,°C$). The $-100\,°C$ test exhibits a dimple morphology and demonstrates the highest ultimate tensile strength of 1231 MPa, along with an excellent elongation of 44%. At high tensile temperatures (650 °C, 750 °C, and 850 °C), the dislocation cutting mechanism and dynamic recrystallization increase the plasticity. However, the presence of a large number of cracks near the spherical primary $L1_2$ phase significantly reduces the ductility and strength. The results show that the hypereutectic $Al_{1.1}CoCrFeNi_{2.1}$ exhibits superior plasticity and strength properties at low temperatures. The findings of the article provide a new approach to enhancing the comprehensive mechanical properties of hypereutectic alloys.

Keywords: hypereutectic; precipitate phase; dynamic recrystallization; mechanical properties

1. Introduction

Yeh et al. in 2004 [1–6], established the concept of high-entropy alloys (HEAs), which were originally defined based on the viewpoint that high-mixing entropy favors the formation of a single solid–solution phase. HEAs contain at least four principal elements with an atomic percentage of 5%–35% [7–10]. HEAs have attracted increased attention due to their desirable properties resulting from a high entropy effect, slow diffusion effect, and cocktail effect [11–15].

From a mechanical standpoint, it is widely acknowledged that single-phased body-centered-cubic (BCC) HEAs possess constrained ductility. Conversely, single-phase face-centered-cubic (FCC) HEAs may possess enhanced ductility but display lower strength [16–19]. Eutectic high-entropy alloys (EHEAs), which contain a mixture of soft FCC and hard BCC phases, can achieve a balance of high strength and ductility, as well as excellent castability [5,20–25]. Among the reported EHEAs, the $AlCoCrFeNi_{2.1}$ alloy, with the combination of a hard phase and soft phase, which contributes to achieving excellent mechanical properties, has attracted the most attention and is considered a potential structural and functional material [26–32].

The $AlCoCrFeNiNi_{2.2}$ hypereutectic high-entropy alloy contains more primary FCC phases. Therefore, the ductility of the $AlCoCrFeNiNi_{2.2}$ hypereutectic high-entropy alloy

is superior to that of the AlCoCrFeNi$_{2.1}$ eutectic high-entropy alloy [33]. Moreover, it is believed that the Al atoms in AlCoCrFeNi-based alloys can lead to the formation of a B$_2$ precipitate phase, and the precipitate guarantees the strength of the alloys [34–37]. The above advantages make it clear that there is great potential for their application in the field of structural materials. However, hypereutectic alloys, which are prepared by increasing the Al content, have been scarcely investigated. Moreover, the influence of the primary FCC phase and B$_2$ precipitate phase on the tensile properties of hypereutectic alloys in a wide temperature range have seldom been studied. Therefore, a novel hypereutectic Al$_{1.1}$CoCrFeNi$_{2.1}$ high-entropy alloy is prepared. This study presents a detailed discussion of the microstructural evolution and mechanical properties of the alloy in a wide temperature range.

2. Materials and Methods

2.1. Material Processing

In this work, the as-cast Al$_{1.1}$CoCrFeNi$_{2.1}$ (at%) high-entropy alloy was prepared in a vacuum magnetic levitation induction furnace. The raw materials of high purity Al, Co, Cr, Fe, and Ni (>99.9 at% pure) were remelted at least 5 times in the Ar atmosphere to guarantee homogeneity.

2.2. Tensile Test

Tensile tests were conducted at $-100\ ^\circ$C (-100-alloy), $23 \pm 2\ ^\circ$C (room temperature, RT-alloy), and elevated temperatures of 650 $^\circ$C (650-alloy), 750 $^\circ$C (750-alloy), and 850 $^\circ$C (850-alloy) in air with a strain rate of 10^{-3} s^{-1}. Dog-bone flat samples with the size of 49 mm × 12 mm were machined from the as-cast samples. The tensile properties were evaluated using a universal testing machine with a strain rate of 0.015 mm/min prior to the yield point and 4.8 mm/min after the yield point. Three parallel samples were tested to obtain the average values of the results.

2.3. Microstructural Characterization

The phase constitution of the alloys was determined by X-ray diffraction (XRD) at 30 kV with Cu Kα radiation. The XRD measurement was conducted at a step size of 4° for a range of 40°–100°. The morphology and microstructure of the alloys were observed by scanning-electron microscopy (SEM). The chemical composition of the alloys was identified using energy dispersive X-ray spectroscopy (EDS). The grain distribution was investigated by SEM, coupled with an electron backscattered diffraction (EBSD) detector. Transmission electron microscopy (TEM) was utilized to identify the microstructure of the alloys.

3. Results

3.1. Microstructure of the As-Cast Alloy

Figure 1 shows the SEM image and XRD pattern of the hypereutectic Al$_{1.1}$CoCrFeNi$_{2.1}$ alloy. The eutectic structures and dendrite structures can be observed in the as-cast condition. Two phases, a white phase (lamellar phase and primary spherical phase) and black phase, exhibit a significant distinction due to the different composition and microstructure, as shown in Figure 1a. The composition of the alloy was 18.12Al-16.01Co-16.11Cr-16.07Fe-33.69Ni (at%) from the EDS results, and the alloy consisted of an FCC and BCC dual-phase from the XRD results (Figure 1b).

Combined with the elemental distributions of the alloy (Figure 2), the white phase was recognized to consist of FCC phases (lamellar and spherical) enriched in Ni, Fe, Co, and Cr elements, whereas the black phase was identified as consisting of BCC enriched in Al and Ni.
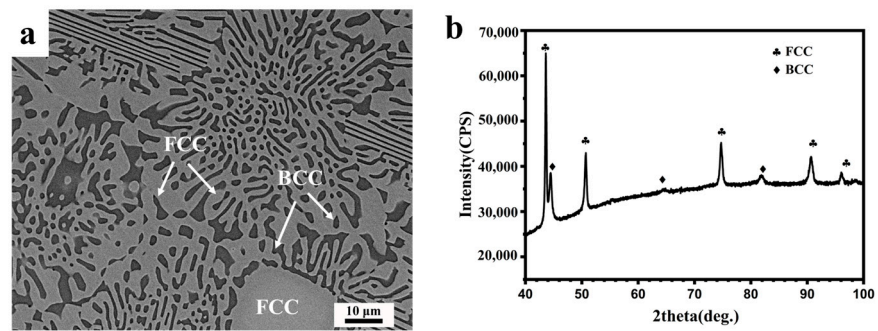
Figure 1. (**a**) SEM image and (**b**) XRD pattern of hypereutectic $Al_{1.1}CoCrFeNi_{2.1}$.
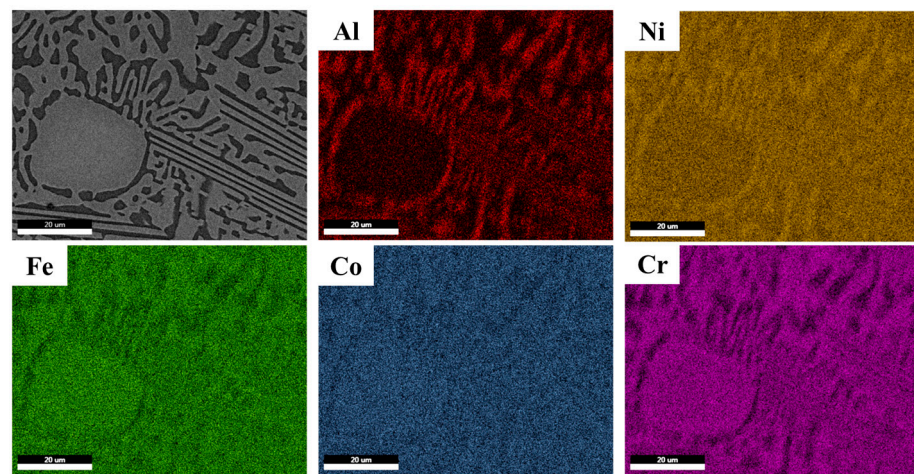
Figure 2. Elemental distributions of the hypereutectic $Al_{1.1}CoCrFeNi_{2.1}$.

Figure 3 gives the TEM images and corresponding selected-area electron diffraction (SEAD) patterns of the as-cast hypereutectic $Al_{1.1}CoCrFeNi_{2.1}$ alloy. The main diffraction spot of the FCC phase is shown in Figure 3a. The presence of superlattice reflections at the {001} position indicates the existence of the $L1_2$-ordered structure. The nano-sized precipitates (in BCC-lamellae) had a B_2 superlattice structure (inset in Figure 3b).
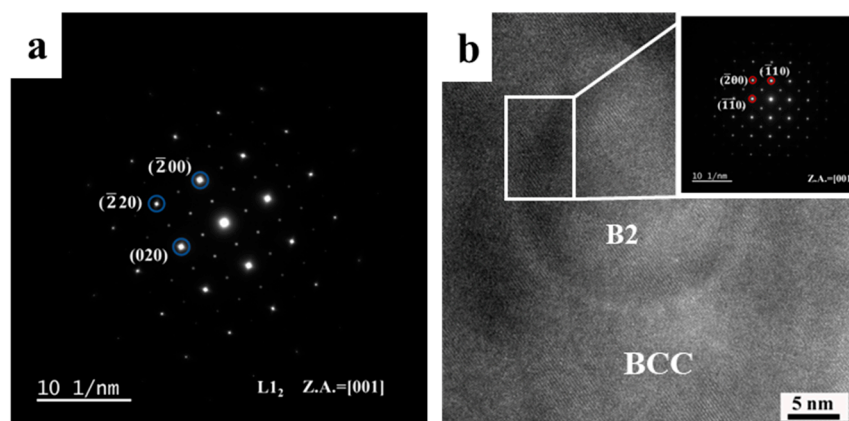
Figure 3. TEM images of $Al_{1.1}CoCrFeNi_{2.1}$: (**a**) SAED corresponding to the $L1_2$; (**b**) HRTEM image of BCC (B2).

3.2. Microstructure of the Alloy after Tensile Tests

To further provide insight into the deformation mechanism, TEM observation of the sample after tension tests (RT-alloy and 650-alloy) was conducted and the results are shown in Figures 4 and 5. As shown in Figure 4a, at room temperature, parallel dislocations appear

in the FCC phases, indicating the occurrence of dislocation slip and cross slip. Meanwhile, the deformation of FCC and BCC (B_2) phases is asynchronous; the BCC (B_2) phase is much harder than the FCC phase. Due to the weaker deformability property of the BCC (B_2) phase, shear bands and shear fractures are observed in the BCC (B_2) phases due to shearing stress concentration, and a high density of dislocations piled up at the shear fracture. From the magnified TEM image of Figure 4b, numerous nano-sized B_2 precipitates are uniformly dispersed in the BCC phases with sizes of about 40 nm.
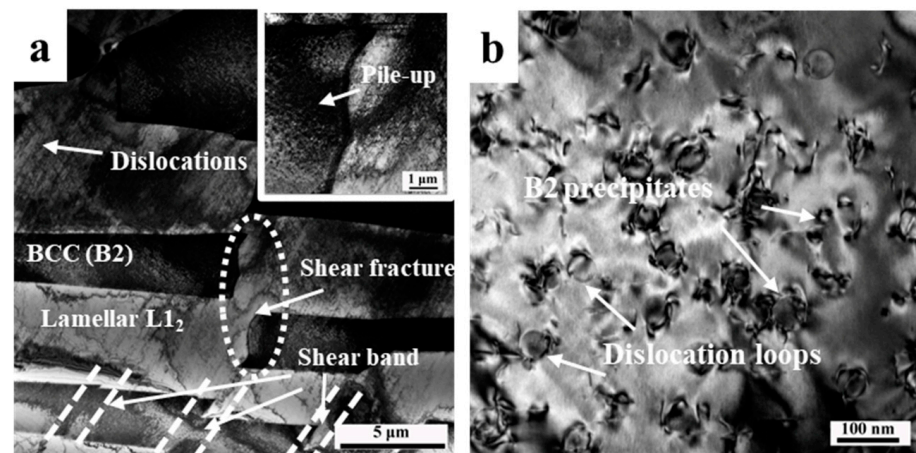
Figure 4. TEM images of RT-alloy: (**a**) low magnification and (**b**) dislocation morphology around B_2 phase.
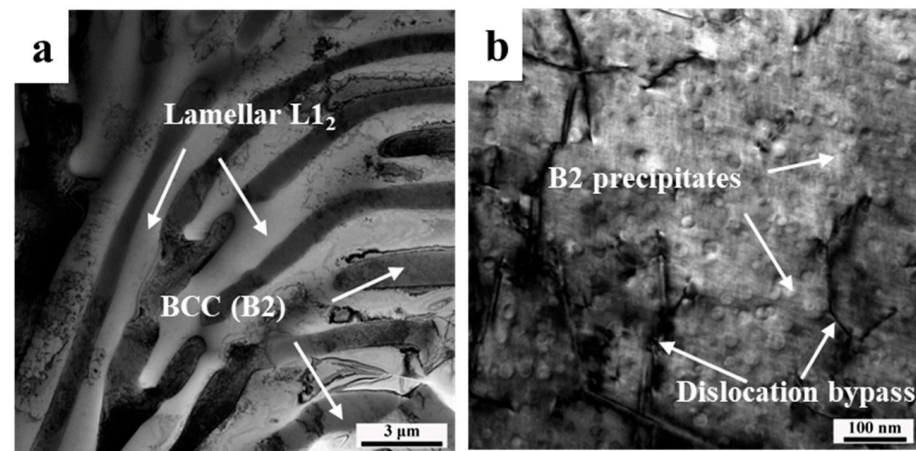
Figure 5. TEM images of 650-alloy: (**a**) low magnification and (**b**) dislocation morphology around B2 phase.

From the 650 °C tensile test (650-alloy), the dislocation density is decreased obviously, and necking is observed for the BCC (B_2) phases. The BCC (B_2) phase undergoes softening and both FCC and BCC (B_2) phases experience severe plastic deformation (Figure 5a). From the magnified TEM image of Figure 5b, numerous nano-sized B_2 precipitates are uniformly dispersed in the BCC phases with sizes of about 20 nm. After the high temperature tension test, the nano-sized precipitates dissolve into the BCC phase, causing a reduction in size.

The EBSD grain distribution maps of the tensile samples for the −100-alloy and RT-alloy are shown in Figure 6. The tensile sample at −100 °C (−100-alloy) exhibits a grain distribution comparable to that of the tensile sample at room temperature (RT-alloy).
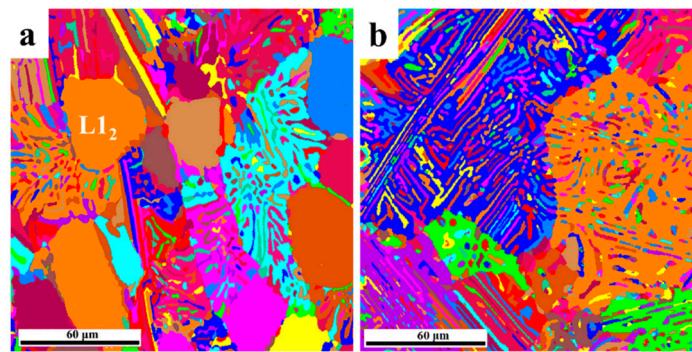
Figure 6. EBSD grain distribution maps of (**a**) −100-alloy; (**b**) RT-alloy.

However, newly formed fine grains in the high-temperature tensile samples were observed, suggesting the occurrence of recrystallisation (Figure 7a–c). The fraction of recrystallized grains increased with increasing tensile temperatures. Recrystallization promotes the dissociation of the dislocation. Since the dissociation of the partial dislocation decreases the dislocation density and reduces the barrier to dislocation movement, the work hardening phenomenon decreases at higher temperatures, and consequently, it promotes the plastic deformation ability. In conclusion, smaller B_2 precipitates and the recrystallization enhanced the collaborative deformation ability of the $L1_2$ and BCC (B_2) phases, which are beneficial to the excellent plastic deformation capacity at high temperatures.
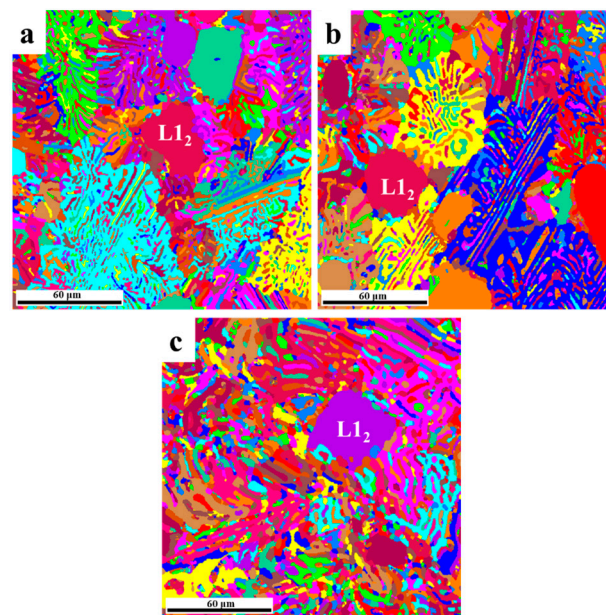
Figure 7. EBSD grain distribution maps of (**a**) 650-alloy; (**b**) 750-alloy; (**c**) 850-alloy.

3.3. Mechanical Properties

The tensile properties of the hypereutectic $Al_{1.1}CoCrFeNi_{2.1}$ alloys are shown in Figure 8. The strain of the alloys increased with increasing tension temperatures. The −100-alloy shows the highest ultimate strength of 1238 MPa. At room temperature, the alloy (RT-alloy) shows an ultimate tensile strength of 964 MPa. At elevated temperatures, there is a significant reduction in strength. The ultimate tensile strength is 455 MPa for the 650-alloy, and 278 MPa for the 750-alloy. The 850-alloy exhibits the lowest ultimate tensile strength, with a value of 156 MPa. Although the plastic deformation capacity exhibits a rising tendency, the strain is still lower than the −100-alloy.
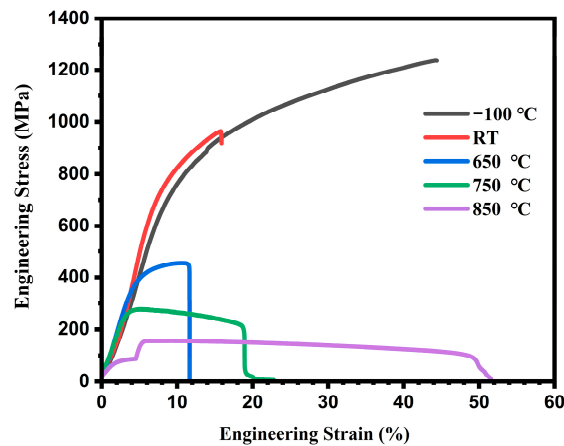
Figure 8. Mechanical properties of hypereutectic $Al_{1.1}CoCrFeNi_{2.1}$ alloy at different temperatures.

To determine the fracture mechanism, typical fracture features of the alloys are observed, as shown in Figure 9. The tensile fractography of the −100-alloy exhibits a large number of dimple morphologies with a minor presence of trench-like morphologies, and no cracks are observed (Figure 9a). The RT-alloy also shows a mixture of trench-like and dimples morphology (Figure 9b). Two different kinds of fracture modes can be clearly distinguished for both the RT-alloy and the −100-alloy: a ductile fracture in the $L1_2$ phase and brittle-like fracture in the BCC (B_2) phase. The incompatibility of strain arising from different levels of elasticity and plasticity between the BCC (B_2) and $L1_2$ phases lead to the local stress concentration. During the tension, the ductile $L1_2$ phase is stretched and then gradually becomes thinner and edged up, whereas the BCC (B_2) phase deforms difficultly and forms a trench bottom. Moreover, many more dimples are observed on the fracture surface of the −100-alloy compared to the RT-alloy, indicating its superior plastic deformation ability.
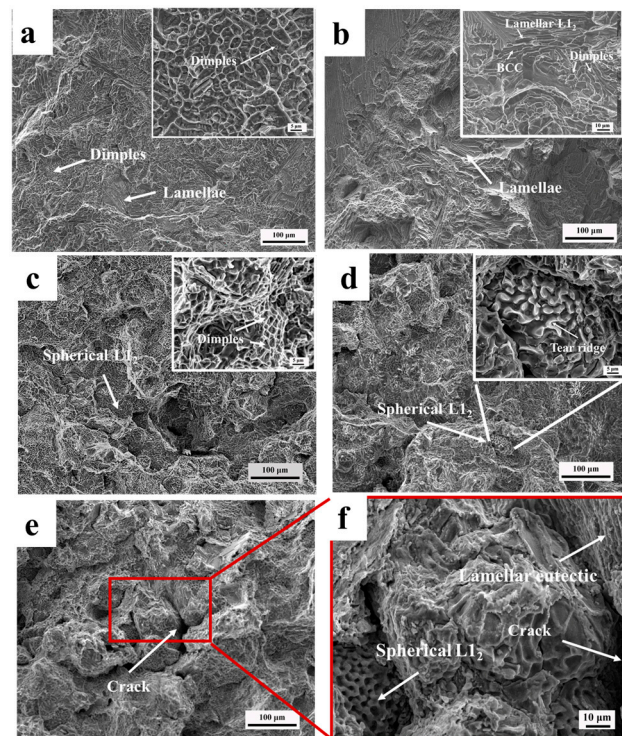
Figure 9. Fracture morphologies of (**a**) −100-alloy; (**b**) RT-alloy; (**c**) 650-alloy; (**d**) 750-alloy; (**e**) 850-alloy; (**f**) magnified spherical $L1_2$ and lamellar eutectic of 850-alloy.

However, for the high-temperature tensile tests, as shown in Figure 9c–f, although numerous dimples also appear (ductile fracture), the cracks observed near the spherical $L1_2$ phase (Figure 9f) significantly reduce the plastic deformation ability.

4. Discussion

With an increasing tensile temperature, the tensile strength decreased. However, the total elongation of the alloys shows an increasing tendency, except for the low-temperature tensile samples (−100-alloy and RT-alloy). The −100 °C test exhibits the highest ultimate tensile strength, along with an excellent elongation. The effect of the tensile temperature on the tensile properties is investigated for the hypereutectic $Al_{1.1}CoCrFeNi_{2.1}$ alloy.

4.1. Synergistic Effect of $L1_2$ and BCC (B_2) Phases

It has been known from earlier studies that the FCC phase ($L1_2$ phase) is more ductile than the BCC (B_2) phase [23]. It seems plausible that the dislocation in the $L1_2$ phase is easier to move than that in the BCC (B_2) phase. A large number of dislocations (dislocation slip and cross slip) are observed within the $L1_2$ phase at room temperature (RT-alloy), as shown in Figure 4a. The deformation of the FCC and BCC (B_2) phases is asynchronous, resulting in the fractures of the BCC (B_2) phases.

The precipitates inhibit the dislocation motion and result in a strengthening effect. Figure 4b shows that the B_2 precipitate phase observed during the deformation process can effectively pin the dislocations through a process known as the Orowan bypass mechanism. When the dislocations approach the precipitates, they start to curve around the non-deformable particles. Under sufficiently applied stress, dislocations may move across the precipitates, leaving behind Orowan loops around the particles (Figure 10a). Dislocation movement can be impeded by the B_2 precipitates, thereby improving the strength for the −100-alloy and RT-alloy.
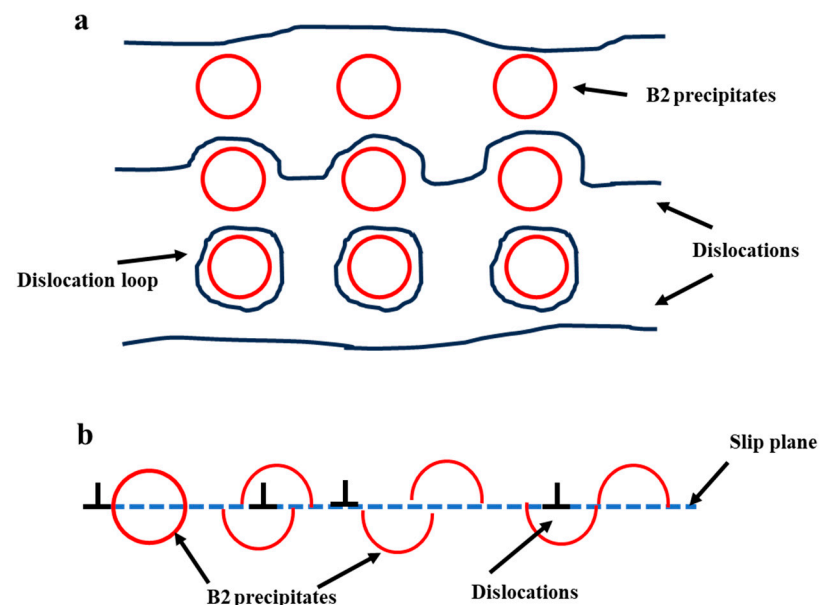
Figure 10. Schematic illustration of (**a**) Orowan bypass mechanism and (**b**) dislocation cutting mechanism.

For the 650-alloy, dislocations are easily cut through by the smaller B_2 precipitates (20 nm), resulting in dislocation slip (Figures 5b and 10b). The dislocation cutting phenomenon is identified as the main mechanism for the softening of the BCC (B_2) phases in the 650-alloy. Softening of the BCC (B_2) phases occurs without shear fracture, and plastic deformation occurs simultaneously in the $L1_2$ and BCC (B_2) phases. Therefore, the ductility increases with increasing tensile temperatures.

However, during high temperature tensile tests, the bonding strength of the spherical primary $L1_2$ and BCC (B_2) phases decreases. The cracks observed near the spherical

L1$_2$ phase significantly reduce the plastic deformation ability and strength. Therefore, the plastic deformation ability of the low temperature tensile tests (-100-alloy) is more outstanding than that of the high temperature tensile tests.

4.2. Dynamic Recrystallization

The alloy undergoes recrystallization during the high-temperature tensile tests. When the dislocation density and driving force reach sufficient levels in the heated, formable alloy, recrystallization takes place. This is because the accelerated diffusion rate of the grain boundaries at high temperatures leads to the continuous growth of sub-grains, ultimately forming new recrystallized grains. In general, when a high temperature collectively ensures the sufficient nucleation time and the high diffusion rate of the grain boundary, dynamic recrystallization occurs. At the same time, the phenomenon of accumulated high-density dislocations disappeare, which improves the plastic deformation ability of the high temperature tensile tests, as shown in Figure 5a.

In conclusion, the Orowan by-passing mechanism and dislocation cutting mechanism affect the dislocation slip. Besides, dynamic recrystallization in the matrix reduces the stress concentration arising from dislocation motion and increases the plastic deformation ability. For the low temperature tensile tests, the Orowan by-passing mechanism caused by the B$_2$ precipitates increase the strength (-100-alloy and RT-alloy). At high temperatures (650-alloy, 750-alloy, and 850-alloy), the dislocation cutting mechanism and dynamic recrystallization increase the plasticity, while the cracks near the spherical L1$_2$ phase significantly reduced the plastic deformation ability.

The Al$_{1.1}$CoCrFeNi$_{2.1}$ hypereutectic high-entropy alloy contains more primary soft FCC phases, which ensure excellent ductility. Moreover, the interaction of the B$_2$ phase and dislocations triggers the Orowan bypass mechanism, thereby contributing to the excellent strength of the alloy. Therefore, compared to other reported hypereutectic high entropy alloys, the alloy studied in this work demonstrates comprehensive mechanical performance advantages [5,19,23].

5. Conclusions

In summary, in this work, hypereutectic Al$_{1.1}$CoCrFeNi$_{2.1}$ alloys were prepared by vacuum magnetic levitation induction melting. Based on the above analysis and results, the main conclusions are as follows:

1. The alloy consisted of L1$_2$ (lamellae and spherical) and BCC (B$_2$) phases. Numerous nano-sized coherent B$_2$ precipitates are uniformly dispersed in the BCC phases. A ductile fracture occurs in the L1$_2$ phase, while a brittle-like fracture occurs in the BCC (B$_2$) phase for both the -100-alloy and RT-alloy.
2. At low tensile temperatures (-100 °C and 23 ± 2 °C), the Orowan by-passing mechanism affects the dislocation slip, contributing to the excellent strength of the alloy. The -100-alloy exhibits the highest ultimate tensile strength of 1231 MPa and excellent elongation of 44%.
3. At high tensile temperatures, the presence of smaller B$_2$ precipitates and the recrystallization resulting from crystallization enhance the collaborative deformation ability of the L1$_2$ and BCC (B$_2$) phase. However, the cracks observed near the spherical primary L1$_2$ phase significantly reduced the plastic deformation ability and strength.

Informed Consent Statement: Not applicable.

Data Availability Statement: Not applicable.

Conflicts of Interest: The authors declare no conflict of interest.

References

1. Semenyuk, A.; Klimova, M.; Shaysultanov, D.; Salishchev, G.; Zherebtsov, S.; Stepanov, N. Effect of nitrogen on microstructure and mechanical properties of the CoCrFeMnNi high-entropy alloy after cold rolling and subsequent annealing. *J. Alloys Compd.* **2021**, *888*, 161452. [CrossRef]
2. Wang, M.L.; Zhang, G.J.; Cui, H.Z.; Lu, Y.; Zhao, Y.; Wei, N.; Li, T. Effect of plasma remelting on microstructure and properties of a CoCrCuNiAl0.5 high-entropy alloy prepared by spark plasma sintering. *J. Mater. Sci.* **2021**, *56*, 5878–5898. [CrossRef]
3. Qi, W.; Wang, W.R.; Yang, X.; Zhang, G.N.; Ye, W.; Su, Y.T.; Li, Y.; Chen, S.Y. Effects of Al and Ti co-doping on the strength-ductility-corrosion resistance of CoCrFeNi-AlTi high-entropy alloys. *J. Alloys Compd.* **2022**, *925*, 166751. [CrossRef]
4. Wu, M.; Yang, C.; Kuijer, M.; Baker, I. Enhanced mechanical properties of carbon-doped FeNiMnAlCr high entropy alloy via hot-rolling. *Mater. Charact.* **2019**, *158*, 109983. [CrossRef]
5. Lu, Y.P.; Gao, X.Z.; Jiang, L.; Chen, Z.; Wang, T.; Jie, J.; Kang, H.; Zhang, Y.; Guo, S.; Ruan, H.; et al. Directly cast bulk eutectic and near-eutectic high entropy alloys with balanced strength and ductility in a wide temperature range. *Acta Mater.* **2017**, *124*, 143–150. [CrossRef]
6. Wang, M.L.; Lu, Y.P.; Zhang, G.J.; Cui, H.; Xu, D.; Wei, N.; Li, T. A novel high-entropy alloy composite coating with core-shell structures prepared by plasma cladding. *Vacuum* **2021**, *184*, 109905. [CrossRef]
7. Sreeram, D.; Pugazhenthi, R.; Anbuchezhiyan, G.; Saravanan, R.; Veeranjaneyulu, K. An investigation of the effects of hot rolling on the microstructure and mechanical behavior of nano-sized SiC particulates reinforced Al6063 alloy composites. *Mater. Today Proc.* **2022**, *64*, 731–736. [CrossRef]
8. Lan, L.; Wang, W.; Cui, Z.; Hao, X.; Qiu, D. Anisotropy study of the microstructure and properties of AlCoCrFeNi$_{2.1}$ eutectic high entropy alloy additively manufactured by selective laser melting. *J. Mater. Res. Technol.* **2022**, *129*, 228–239. [CrossRef]
9. Choudhuri, D.; Shukla, S.; Jannotti, P.A.; Muskeria, S.; Mukherjee, S.; Lloydc, J.T.; Mishra, R.S. Characterization of as-cast microstructural heterogeneities and damage mechanisms in eutectic AlCoCrFeNi$_{2.1}$ high entropy alloy. *Mater. Charact.* **2019**, *158*, 109955. [CrossRef]
10. Duan, X.T.; Han, T.Z.; Guan, X.; Wang, Y.N.; Su, H.H.; Ming, K.S.; Wang, J.; Zheng, S.J. Cooperative effect of Cr and Al elements on passivation enhancement of eutectic high-entropy alloy AlCoCrFeNi$_{2.1}$ with precipitates. *J. Mater. Res. Technol.* **2023**, *136*, 97–108. [CrossRef]
11. Peng, P.; Li, S.Y.; Chen, W.Q.; Xu, Y.L.; Zhang, Z.D.; Ma, Z.K.; Wang, J.T. Phase selection and mechanical properties of directionally solidified AlCoCrFeNi$_{2.1}$ eutectic high-entropy alloy. *J. Alloys Compd.* **2022**, *898*, 162907. [CrossRef]
12. Wang, J.R.; Jiang, F.; Wang, L.; Yang, G.J.; Xu, M.Q.; Yi, J.J. Cr addition-mediated simultaneous achievement of excellent strength and plasticity in non-equiatomic Nb-Ti-Zr-Ta-base refractory high-entropy alloys. *J. Alloys Compd.* **2023**, *946*, 169423. [CrossRef]
13. Nguyen, V.T.; Qian, M.; Shi, Z.; Tran, X.Q.; Fabijanic, D.M.; Joseph, J.; Qu, D.D.; Matsumura, S.; Zhang, C.; Zhang, F.; et al. Cuboid-like nanostructure strengthened equiatomic Ti–Zr–Nb–Ta medium entropy alloy. *Mater. Sci. Eng. A* **2020**, *798*, 140169. [CrossRef]
14. Iijima, Y.; Nagase, T.; Matsugaki, A.; Wang, P.; Ameyama, K.; Nakano, T. Design and development of Ti–Zr–Hf–Nb–Ta–Mo high-entropy alloys for metallic biomaterials. *Mater. Des.* **2021**, *202*, 109548. [CrossRef]
15. Yang, W.; Pang, S.; Liu, Y.; Wang, Q.; Liaw, P.K.; Zhang, T. Design and properties of novel Ti–Zr–Hf–Nb–Ta high-entropy alloys for biomedical applications. *Intermetallics* **2022**, *141*, 107421. [CrossRef]
16. Cao, Y.; Liu, Y.; Liu, B.; Zhang, W. Precipitation behavior during hot deformation of powder metallurgy Ti-Nb-Ta-Zr-Al high entropy alloys. *Intermetallics* **2018**, *100*, 95–103. [CrossRef]
17. Eleti, R.R.; Stepanov, N.; Yurchenko, N.; Klimenko, D.; Zherebtsov, S. Plastic deformation of solid-solution strengthened Hf-Nb-Ta-Ti-Zr body-centered cubic medium/high-entropy alloys. *Scr. Mater.* **2021**, *200*, 113927. [CrossRef]
18. Xiang, T.X.; Du, P.; Cai, Z.Y.; Li, K.; Bao, W.Z.; Yang, X.X.; Xie, G.Q. Phase-tunable equiatomic and non-equiatomic Ti-Zr-Nb-Ta high-entropy alloys with ultrahigh strength for metallic biomaterials. *J. Mater. Sci. Technol.* **2022**, *117*, 196–206. [CrossRef]
19. Nagase, T.; Todai, M.; Hori, T.; Nakano, T. Microstructure of equiatomic and non-equiatomic Ti-Nb-Ta-Zr-Mo high-entropy alloys for metallic biomaterials. *J. Alloys Compd.* **2018**, *753*, 412–421. [CrossRef]
20. Zhang, Y.L.; Wang, X.G.; Li, J.G.; Huang, Y.Q.; Lu, Y.P.; Sun, X.F. Deformation mechanism during high-temperature tensile test in an eutectic high-entropy alloy AlCoCrFeNi$_{2.1}$. *Mater. Sci. Eng. A* **2018**, *724*, 148–155. [CrossRef]
21. Peng, P.P.; Feng, X.N.; Li, S.Y.; Wei, B.L.; Zhang, M.Y.; Xu, Y.L.; Zhang, Z.D.; Ma, Z.K.; Wang, J.T. Effect of heat treatment on microstructure and mechanical properties of as-cast AlCoCrFeNi$_{2.1}$ eutectic high entropy alloy. *J. Alloys Compd.* **2023**, *939*, 168843. [CrossRef]
22. Lan, L.X.; Yang, Z.Y.; Wang, W.S.; Cui, Z.Q.; Hao, X.H. Effect of initial powder particle size on densification behavior and mechanical properties of laser additive manufacturing of AlCoCrFeNi$_{2.1}$ eutectic high-entropy alloy. *Powder Technol.* **2023**, *420*, 118379. [CrossRef]

23. Bhattacharjee, T.; Zheng, R.; Chong, Y.; Sheikh, S.; Guo, S.; Clark, I.T.; Okawa, T.; Wani, I.S.; Bhattacharjee, P.P.; Shibata, A.; et al. Effect of low temperature on tensile properties of AlCoCrFeNi$_{2.1}$ eutectic high entropy alloy. *Mater. Chem. Phys.* **2018**, *210*, 207–212. [CrossRef]

24. Zhang, X.B.; Li, B.; Zeng, L.; Yi, J.J.; Wang, B.Q.; Hu, C.H.; Xia, M.X. Effect of Re addition on the microstructure and mechanical properties of AlCoCrFeNi$_{2.1}$ eutectic high-entropy alloy. *Intermetallics* **2023**, *154*, 107808. [CrossRef]

25. Shim, S.H.; Pouraliakbar, H.; Minouei, H.; Rizi, M.S.; Fallah, V.; Na, Y.S.; Han, J.H.; Hong, S.I. Characterization of the microscale/nanoscale hierarchical microstructure of an as-cast CrMnFeNiCu high-entropy alloy with promising mechanical properties. *J. Alloys Compd.* **2023**, *954*, 170091. [CrossRef]

26. Feng, J.J.; Gao, S.; Han, K.; Miao, Y.D.; Qi, J.Q.; Wei, F.X.; Ren, Y.J.; Zhan, Z.Z.; Sui, Y.W.; Sun, Z.; et al. Effects of minor B addition on microstructure and properties of Al$_{19}$Co$_{20}$Fe$_{20}$Ni$_{41}$ eutectic high-entropy alloy. *Trans. Nonferrous Met. Soc. China* **2021**, *31*, 1049–1058. [CrossRef]

27. Zhang, M.N.; Wang, D.F.; He, L.J.; Ye, X.Y.; Zhang, W.W. Laser beam welding of AlCoCrFeNi$_{2.1}$ eutectic high-entropy alloy. *Mater. Lett.* **2022**, *308*, 131137. [CrossRef]

28. Wischi, M.; Campo, K.N.; Starck, L.F.; Da Fonseca, E.B.; Lopes, N.; Caram, R. Microstructure and mechanical behavior of the directionally solidified AlCoCrFeNi$_{2.1}$ eutectic high-entropy alloy. *J. Mater. Res. Technol.* **2022**, *20*, 811–820. [CrossRef]

29. Wang, S.; Li, Y.; Zhang, D.; Yang, Y.; Marwana, M.S.; Luo, Z. Microstructure and mechanical properties of high strength AlCoCrFeNi$_{2.1}$ eutectic high entropy alloy prepared by selective laser melting (SLM). *Mater. Lett.* **2022**, *310*, 131511. [CrossRef]

30. Gao, X.J.; Wang, L.; Guo, N.N.; Luo, L.S.; Zhu, G.M.; Shi, C.C.; Su, Y.Q.; Guo, J.J. Microstructure and mechanical properties of multi-phase reinforced Hf-Mo-Nb-Ti-Zr refractory high-entropy alloys. *Int. J. Refract. Met. Hard Mater.* **2022**, *102*, 105723. [CrossRef]

31. Hou, J.X.; Tan, Y.; Liu, S.F.; Zhang, J.Y.; Xiao, W.C.; Kong, H.J.; Li, Q.; Cao, B.X.; Luan, J.H.; Zhao, Y.L.; et al. High-temperature oxidation behaviors and mechanisms in newly designed L12-strengthened high-entropy alloys. *Corros. Sci.* **2022**, *208*, 110665. [CrossRef]

32. Kireeva, I.V.; Chumlyakov, Y.I.; Pobedennaya, Z.V.; Vyrodova, A.V. Effect of γ'-phase particles on the orientation and temperature dependence of the mechanical behaviour of Al$_{0.3}$CoCrFeNi high-entropy alloy single crystals. *Mater. Sci. Eng. A* **2020**, *772*, 138772. [CrossRef]

33. Huang, X.; Dong, Y.; Lu, S.M.; Li, C.Q.; Zhang, Z.G. Effects of Homogenized Treatment on Microstructure and Mechanical Properties of AlCoCrFeNi$_{2.2}$ Near-Eutectic High-Entropy Alloy. *Acta. Metall. Sin.* **2021**, *34*, 1079–1086. [CrossRef]

34. Hayun, S.; Lilova, K.; Salhov, S.; Navrotsky, A. Enthalpies of formation of high entropy and multicomponent alloys using oxide melt solution calorimetry. *Intermetallics* **2020**, *125*, 106897. [CrossRef]

35. Li, C.; Zhao, M.; Li, J.C.; Jiang, Q. B2 structure of high-entropy alloys with addition of Al. *J. Appl. Phys.* **2008**, *104*, 113504. [CrossRef]

36. Jin, X.; Bi, J.; Zhang, L.; Zhou, Y.; Du, X.Y.; Yuxin Liang, Y.X.; Li, B.S. A new CrFeNi$_2$Al eutectic high entropy alloy system with excellent mechanical properties. *J. Alloys Compd.* **2019**, *770*, 655–661. [CrossRef]

37. Wang, L.; Su, Y.N.; Yao, C.L.; Huang, Y.D.; Shen, J.; Zhang, Y.P.; Liu, G.; Zhao, P.K.; Zhang, G.J. Microstructure and mechanical property of novel NiAl-based hypoeutectic/eutectic/hypereutectic high-entropy alloy. *Intermetallics* **2022**, *143*, 107476. [CrossRef]